(Preprint) AAS 24-189

ELECTROSTATIC TRACTOR EFFECTIVENESS IN A NON-MAXWELLIAN GEO PLASMA ENVIRONMENT

Amy Haft* and Hanspeter Schaub†

The electrostatic tractor has been proposed as a promising contactless method to dispose of large defunct spacecraft in Geosynchronous Earth Orbit. Here, a servicer spacecraft equipped with an electron gun directs the electron beam at a target, charging it negative, while the emission of electrons charges the serciver positively. An attractive electrostatic force between the two spacecraft allows the servicer to reorbit the target into a graveyard orbit. While the electrostatic tractor has been studied in a Maxwellian plasma, suprathermal particle deviations from the Maxwellian distribution function, which exist in every low-density plasma environment, influence the controlled spacecraft charging induced by the electrostatic tractor. This paper expands on electrostatic space debris mitigation research by investigating and comparing active charging in non-Maxwellian GEO environments using three alternate distribution models: (1) bi-Maxwellian distribution, (2) kappa function, and (3) cool Maxwellian core with a hot kappa halo. The forces and torques are then computed from the resulting equilibrium potentials using the multi-sphere method to demonstrate the full impact the environments have on the effectiveness of the electrostatic tractor.

INTRODUCTION

For satellites in Geostationary Earth Orbit (GEO), debris mitigation guidelines set by the Inter-Agency Space Debris Coordination Committee (IADC) suggest a minimum graveyard orbit of a few hundred kilometers beyond the operational orbit, including 235km to account for the GEO-protected zone and gravitational perturbations added to the effect of solar radiation pressure on the spacecraft.[1] However, data collected between 1997 and 2013 shows that only about 50% of GEO satellites worldwide complied with IADC guidelines, while about 30% failed to meet guidelines and another 20% were abandoned.[2] In the United States, the Federal Communications Commission (FCC) established that all satellites launched after March 18, 2002 must commit to a minimum altitude boost of 300km at the end of their operational lives,[3] but repercussions for non-compliant satellites were not enacted until 2023.[4] The significant insurance value of GEO satellites[2] highlights the importance of those assets, and the increasing risk of collisions in the GEO regime[5,6] due to congestion from non-compliant satellites could have detrimental impacts on communications, broadcasting, commerce, and Earth-observing activities.

To avoid potential collisions, Active Debris Removal (ADR) in GEO is necessary. Many proposed methods of ADR in Low Earth Orbit (LEO) involve physical contact or grappling with the target debris object.[7–12] However, defunct GEO satellites have been observed to tumble with spin rates

*Graduate Research Assistant, Ann and H.J. Smead Department of Aerospace Engineering Sciences, Colorado Center for Astrodynamics Research, AIAA Student Member, Email: amy.haft@colorado.edu.

†Professor and Department Chair, Schaden Leadership Chair, Ann and H.J. Smead Department of Aerospace Engineering Sciences, Colorado Center for Astrodynamics Research. AAS Fellow, AIAA Fellow.

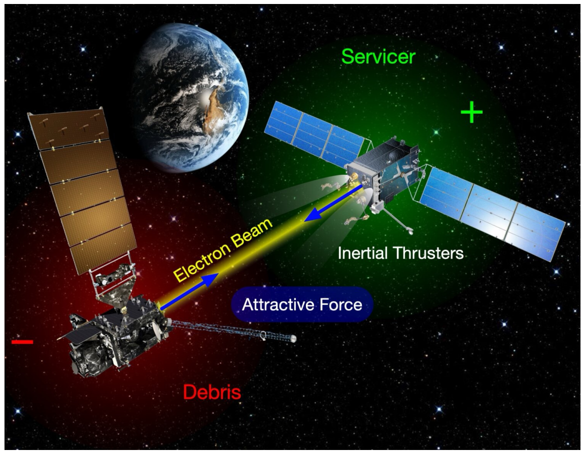

Figure 1: Electrostatic Tractor Concept

reaching many 10s deg/s,[13,14] making it very difficult to physically grapple with or detumble the debris.[15] The electrostatic tractor was proposed in 2012 as a contactless method of ADR in GEO.[16] Here, an electron beam is mounted onto a servicer spacecraft. The electron beam is directed at a target spacecraft, resulting in electron beam emission from the servicer and electron beam impact on the target. With this flow of electrons, the servicer is charged positively and the target should be charged negatively to initiate an attractive electrostatic force between the spacecraft, which would allow the servicer to pull the target into a graveyard orbit. The Debye lengths, a measure of how far a charge's electrostatic effect persists, of several hundreds of meters in the GEO space environment (compared to centimeters in LEO) ensure that potential shielding due to the ambient plasma is not a concern.[17]

The GEO space environment is volatile and susceptible to geomagnetic substorms every few hours,[18] which may greatly affect active charging using the electron beam. During a substorm, the Earth's magnetotail snaps back from its extended local nighttime position and sends electrons and ions accelerating back toward Earth. Many of these highly energized particles are injected into GEO. Because the nominal plasma at GEO is rarified and collisionless, the sudden injection of high-energy plasma during substorms every few hours[18] frequently makes the environment a mixture of two different plasmas. Earth's magnetosphere can also be compressed during geomagnetic storms. In a worst-case scenario known as "The Great Magnetic Storm" that occured on March 13, 1989, the magnetopause was compressed from $10\mathrm{R_E}$ to inside GEO at $6.6\mathrm{R_E}$[19] such that GEO satellites were directly exposed to the solar wind. While geomagnetic storms at this level of severity are rare, occurring only every few decades, the compression of the magnetosphere during any period of geomagnetic activity can result in non-thermal distributions in the plasma at GEO. Suprathermal deviations from the Maxwellian velocity distribution function (VDF) are expected to exist in any low-density plasma,[20] meaning that even during quiet periods, the plasma at GEO may be better represented using a non-Maxwellian VDF. Non-thermal particle distributions in the solar-wind and near-Earth space plasma have been confirmed by several interplanetary missions.[21–25]

In this paper, the GEO environment is modeled using several non-Maxwellian VDFs to represent various environments. First, charging using a bi-Maxwellian VDF, which models the environment as a mixture of two distinct plasmas, is reviewed. Then, a generalized Lorentzian, or kappa, VDF models the environment during quiet periods and when exposed fully to the solar wind. The sum

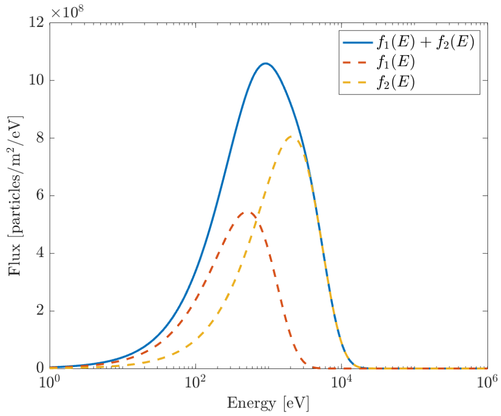

(a) Electron flux in the mild bi-Maxwellian environment

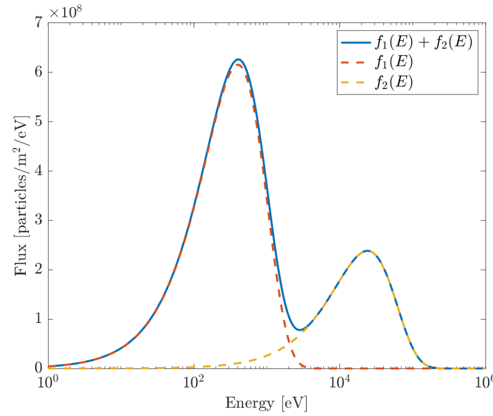

(b) Electron flux in the worst-case environment

Figure 2: Electron flux vs. Energy in two bi-Maxwellian environments

of a Maxwellian core and kappa halo will also be explored as an interesting model where a bi-Maxwellian VDF is a particular case. The forces and torques from the resulting potentials will be modeled to show the effectiveness of the electrostatic tractor for each environment.

SPACECRAFT CHARGING IN BI-MAXWELLIAN PLASMA

Particle Flux

A bi-Maxwellian plasma is a combination of two plasmas that are each represented using a Maxwellian VDF. Therefore, the VDF for a bi-Maxwellian plasma $f(E)$ is simply the sum of two distinct Maxwellian VDFs, $f_1(E)$ and $f_2(E)$, such that[26]

$$f(E) = f_1(E) + f_2(E) \tag{1a}$$

$$f_1(E) = n_1 \left(\frac{q_0}{2\pi m T_1} \right)^{1/2} \frac{E}{T_1} \exp\left(-\frac{E}{T_1} \right) \tag{1b}$$

$$f_2(E) = n_2 \left(\frac{q_0}{2\pi m T_2} \right)^{1/2} \frac{E}{T_2} \exp\left(-\frac{E}{T_2} \right) \tag{1c}$$

where the energy E is related to the particle mass m and velocity v using $E = \frac{1}{2}mv^2$, and the subscripts 1 and 2 denote the respective values of number density n and temperature T for electron population 1 and 2. The temperature T in Equation (1) is in units of electron volts (eV) and the charge of the particle is denoted by the constant q_0. The VDF used here is a measure of the flux of the plasma in units of paricles/m^2/eV. It is noted that $T_2 > T_1$ and represents the suprathermal deviation from the Maxwellian.

The bi-Maxwellian VDF described in Equation (1) is illustrated in Figure 2. The total electron flux $f_1(E) + f_2(E)$ is shown as a solid blue curve, while the Maxwellian fluxes of each population, $f_1(E)$ and $f_2(E)$, are shown as red and yellow dashed curves, respectively. The two graphs in the Figure show the flux result for different environments. Figure 2a shows the flux for a more mild bi-Maxwellian environment, with parameters shown in Table 1. The particle densities and temperatures were chosen with respect to typical GEO environment parameters during quiet periods just before a

Table 1: Mild Bi-Maxwellian Environment

Particle Type	Parameter			
	T_1 (keV)	T_2 (keV)	n_1 (cm^{-3})	n_2 (cm^{-3})
Electron	0.5105	2.1	0.2	0.6
Ion	0.5105	2.1	0.2	0.6

Table 2: SCATHA Worst-Case Environment[27]

Particle Type	Parameter			
	T_1 (keV)	T_2 (keV)	n_1 (cm^{-3})	n_2 (cm^{-3})
Electron	0.4	24	0.2	0.6
Ion	0.3	26	1.6	0.6

geomagnetic substorm (at around local midnight) and during a geomagnetic substorm (during local dawn hours).[28] For simplicity, the ion temperatures were set equal to the electron temperatures. It can be seen in Figure 2a that the shape of the $f_1(E) + f_2(E)$ curve is roughly Maxwellian. In Figure 2b, which uses the parallel SCATHA worst-case measurements from April 24, 1978,[27] the $f_1(E) + f_2(E)$ curve appears almost as two distinct Maxwellian curves due to the significant temperature disparity between population 1 and population 2.

Charging Threshold

It was previously discovered that, for a single-Maxwellian plasma, a target spacecraft in an eclipse being actively charged using an electron beam will have 3 equilibrium potentials.[29] An equilibrium potential is the electric potential of a charged object at which the net current acting on the object is zero. Of the 3 equilibria, the most and least negative potentials are stable while the middle one is unstable. Because of this, any sufficiently large deviation from a stable point will cause the spacecraft potential to jump to the other stable equilibrium. This result closely emulates the triple-root jump phenomenon that occurs naturally in a bi-Maxwellian plasma. The triple-root jump is the sudden jump from a stable negative equilibrium potential to a stable positive equilibrium potential through an unstable third root as a result of perturbations in the environment. This concept was first proposed in 1965[30] and confirmed experimentally in 1988.[31]

The onset of charging in any space environment is characterized by a charging threshold. This threshold in a single-Maxwellian plasma is simply the critical temperature T^* for a given material, which is found by solving the current balance for an initially uncharged spacecraft in an environment where the ion contribution is neglected. Using the Sanders and Inouye secondary electron formula[32]

$$\delta(E) = c[\exp(-E/a) - \exp(-E/b)] \tag{2}$$

and the Prokopenko and Laframboise backscattered electron formula[33]

$$\eta(E) = A - B\exp(-CE) \tag{3}$$

where $a = 4.3E_{\text{max}}$, $b = 0.367E_{\text{max}}$, and $c = 1.37\delta_{\text{max}}$ and A, B, and C depend on the surface materials, the threshold condition can be written as[34]

$$c\left[(1 + k_BT/a)^{-2} - (1 + k_BT/b)^{-2}\right] + A - B(1 + Ck_BT)^{-2} = 1. \tag{4}$$

The solution T to Equation (4) is either the anticritical temperature T_A or the critical temperature T^* for the material and $T^* > T_A$. In this paper, the material used is silver due to its consistent material properties across other sources[34,35] and the NASCAP documentation.[26] The material properties for silver are a = 3.44, b = 0.2936, c = 1.37, A = 0.39, B = 0.2890, and C = 0.6320. For simplicity the threshold condition will be written using the following shorthand notation:[36]

$$< \delta(E) + \eta(E) >= 1. \tag{5}$$

The charging threshold in a bi-Maxwellian plasma is significantly more complex. For an initially uncharged spacecraft $\phi_0 = 0$ in an environment neglecting the ion contribution, the current balance is

$$\int_0^\infty (f_1(E) + f_2(E))E\mathrm{d}E = \int_0^\infty (f_1(E) + f_2(E))E[\delta(E) + \eta(E)]\mathrm{d}E \tag{6}$$

After complex algebra and substituting in the required equations, Equation (6) becomes

$$\frac{\alpha(k_BT_1)^{1/2} < \delta(E) + \eta(E) >_1 + (k_BT_2)^{1/2} < \delta(E) + \eta(E) >_2}{\alpha(k_BT_1)^{1/2} + (k_BT_2)^{1/2}} = 1 \tag{7}$$

where $\alpha = n_1/n_2$. Huang et. al show this derivation in greater detail.[36] From Equation (7), it is evident that the threshold condition in a bi-Maxwellian plasma is now dependent on 4 parameters: n_1, n_2, T_1, and T_2. As $\alpha \to \infty$, the plasma behaves like a single-Maxwellian plasma.

In a more realistic space environment that includes the contributions from other current sources including ions, it is easier to solve for the threshold numerically using a spacecraft charging model. The charging model used in this paper was developed by J. Hammerl and H. Schaub[29] in Ref. 29. The model assumes a spherical, fully-conducting spacecraft such that all charging occurs on the surface and there is only one electric potential ϕ across the entire surface. The radii of the servicer and target spacecraft are set to $R_S = R_T = 1$m, and the secondary and backscattered electron yields due to the incoming electron current are modeled by Equation (2) and Equation (3) for consistency across previous bi-Maxwellian research.[34,36,37] The other equations remain the same.

Figure 3 compares the bi-Maxwellian charging threshold curve for silver using the analytical solution and numerical solution. The blue, U-shaped curve represents the charging threshold. In the shaded region above the U-shaped curve, the spacecraft potential will converge to a positive value. Outside of the shaded region, the spacecraft will be charged negatively. The yellow, dotted curve shows the threshold condition for a single-Maxwellian plasma. For the single-Maxwellian threshold curve, the y-axis is the value of $< \delta + \eta >$ calculated using Equation (4). The first temperature at which the curve crosses 1 is the anticritical temperature T_A and the second temperature is the critical temperature T^*. In Figure 3a, the asymptotes of the bi-Maxwellian threshold curve are at T_A and T^*. Recall that the analytical solution in Figure 3a assumes that the spacecraft is initially uncharged $\phi_0 = 0$ and neglects the ion contribution from the environment. The numerical solution in Figure 3b also follows a U-shape, but does not have asymptotes at T_A and T^*. In the space environment used in this figure, the ambient ion temperatures and densities are equal to the ambient electron temperatures, which are shown in the graph as T_1, T_2, and α. Increasing the ion temperatures and densities affects the threshold curve by decreasing the required population 1 electron temperature T_1 and electron density ratio α to induce a potential jump, thus shifting the curve to the left and down. Denser, hotter ion populations make the spacecraft potential more likely to jump from negative to

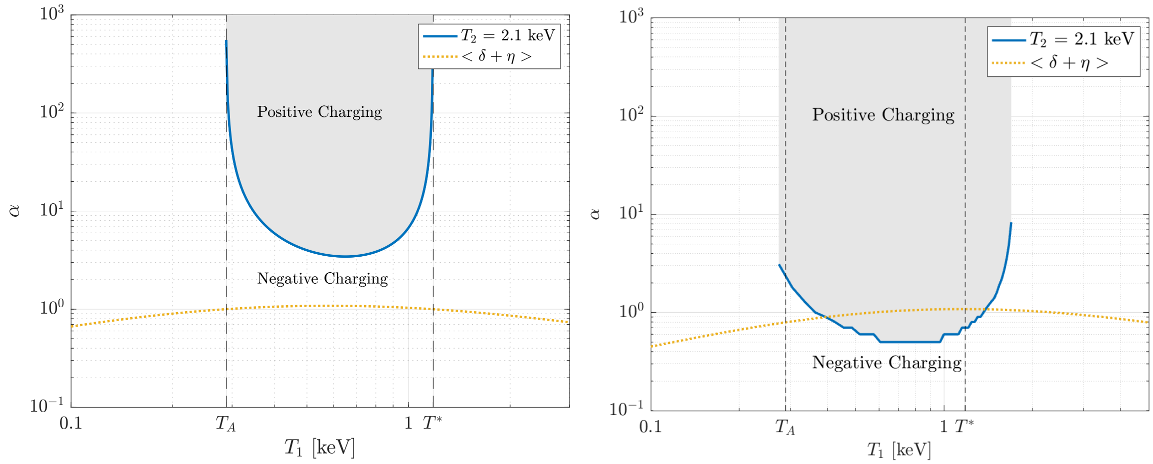

(a) Analytical solution with $\phi_0 = 0$ and no ions **(b)** Numerical solution using spacecraft charging model

Figure 3: Bi-Maxwellian charging threshold curves

positive due to the intense ion contribution on the spacecraft. For both Figures 3a and 3b, increasing T_2 would shift the curve up, meaning that a higher α is required to induce a jump from negative to positive. Another key finding is that the charging threshold in a bi-Maxwellian environment using the charging model does not depend on the initial spacecraft potential ϕ_0. In other words, regardless of ϕ_0, the spacecraft will jump from negative to positive (or vice versa) at the same values of α, T_1, and T_2. Additionally, for a given environment, the positive and negative equilibrium potentials will be the same for any ϕ_0.

Active Spacecraft Charging

Figure 4 shows the result of active charging on the target in the mild spacecraft environment shown in Table 1, accounting for the effects of the servicer with an electron beam current $I_{\text{beam}} = 50\mu$A. The target is assumed to be fully eclipsed by the servicer, which is fully exposed to the sun. Additionally, n_2 varies with α as $n_2 = \alpha/n_1$. Figure 4a illustrates the target potential over time at 10 linearly spaced initial target potentials ϕ_0. For each ϕ_0, 50 linearly spaced values of α ranging from 0.1 to 10 are plotted. Values of $\alpha > 1$ are shown in orange, and values of $\alpha < 1$ are shown in blue. Figure 4b illustrates the effect of α on the negative equilibrium potentials of the target. An equilibrium potential occurs when the net current acting on the spacecraft is equal to zero, $I_{\text{net}} = 0$A. In Figure 4b, the surface plot is colored green when the net current is greater than zero and colored red when the net current is less than zero. The equilibrium potentials occur at the intersection of the green and red surfaces. The black points on the curve highlight the equilibrium potentials at $\alpha = 10$. The least negative equilibrium potential is generated from the impact of the electron beam on the target and the resulting secondary and backscattered electrons. It can be observed in Figure 4a that this equilibrium is at a greater potential than ϕ_0 for most ϕ_0. This is a result of both the environmental conditions and the charging of the servicer. In the natural environment, the target would be charged slightly positive, thus the environment has a positive influence on the charging of the target. The servicer is also initially charged positively and the electron beam emission causes it to charge even more positively. As a result, the electrons become more attracted to the servicer over time until equilibrium is reached. Therefore, the impact of the electron beam on the target decreases

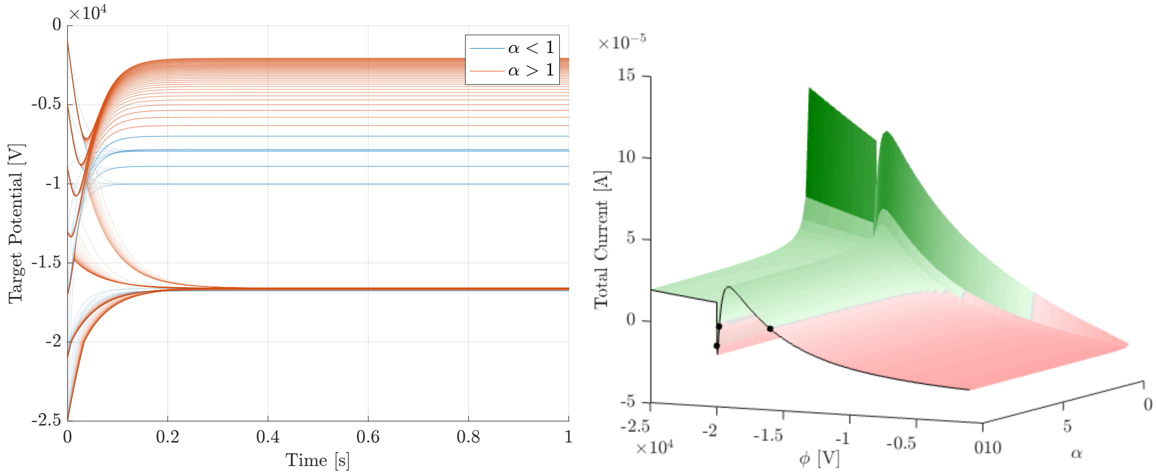

(a) Target potential vs. time

(b) Total current vs. potential and electron density ratio

Figure 4: Active charging in mild bi-Maxwellian environment

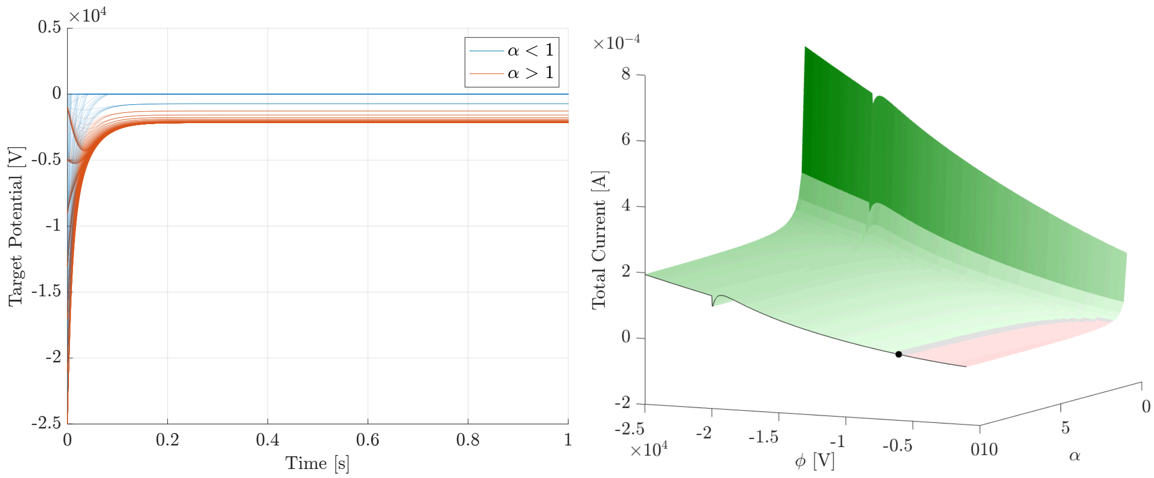

(a) Target potential vs. time

(b) Total current vs. potential and electron density ratio

Figure 5: Active charging in SCATHA worst-case environment

over time and creates the reversal of charging seen in Figure 4a. The most negative equilibrium potential corresponds to the case where the target is initially charged so negatively that the electron beam cannot reach it. Without the servicer, the equilibrium potential would be equal to negative the electron beam energy, which in this case is 20keV. However, with the servicer included, the positive influence of the environment brings this potential to a less negative value. In some cases, the target begins to charge positively, but sharply reverses and charges negatively to converge to the most negative equilibrium potential. Since the electron beam cannot initially reach the target, it charges positively due to the influence of the environment. It quickly reaches a less negative potential that allows for the impact of the electron beam, and the target potential converges to the most negative equilibrium potential.

The effect of varying α on the least negative equilibrium potential is apparent in both Figures 4a and 4b. When $\alpha < 1$, perturbations in the environment density can cause the target potential to jump thousands of volts. As $\alpha \to 0$, the effect of perturbations becomes more significant. However, as $\alpha \to \infty$, the plasma behaves like a Maxwellian plasma, and the target potential converges to a particular value. The electrostatic tractor would consequently be most predictable and effective in an environment where α is large, such that $n_1 \gg n_2$.

Figure 5 shows the result of active charging on the target in the SCATHA worst-case environment shown in Table 2, accounting for the effects of the servicer. Again, the target is assumed to be fully eclipsed by the servicer, which is fully exposed to the sun, and n_2 varies with α as $n_2 = \alpha/n_1$. Figure 5b shows that each value of α has only 1 equilibrium potential, rather than 3 as was the case for the mild environment. In Figure 5a, it can be observed that a jump to a positive potential is possible in this environment for small values of α. This would be detrimental to the performance of the electrostatic tractor and serves as an example of why operating in low α environments could be complicated. It should be noted that the element of the environment that generates this result is the 8:1 ratio of population 1 ion density to population 1 electron density $n_{i_1} : n_1$. The large contribution from the ion current compared to electron current exerts a substantial positive influence on the charging of the spacecraft, resulting in the possibility of a jump to a positive potential.

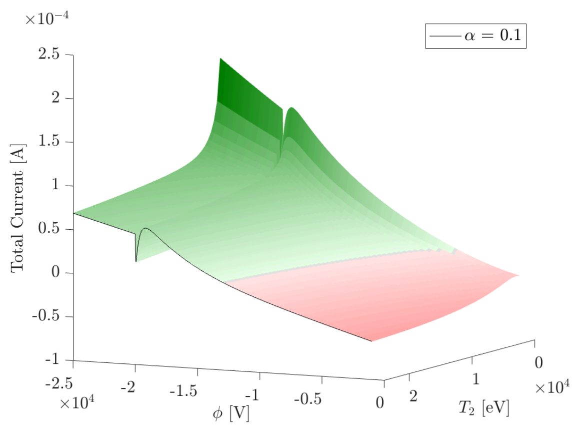

(a) For $\alpha = 0.1$

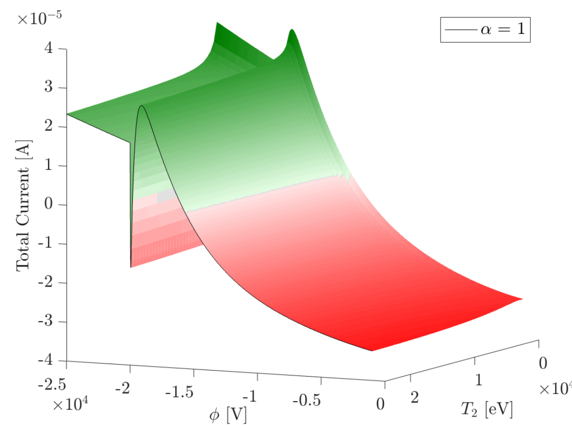

(b) For $\alpha = 1$

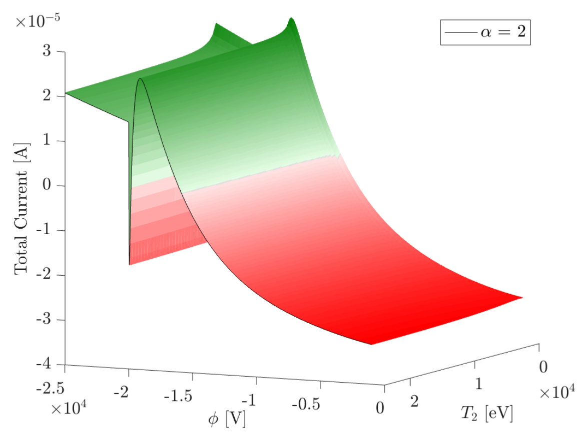

(c) For $\alpha = 2$

Figure 6: Total current vs. potential and T_2 for various values of α

Figure 6 shows the equilibrium surface plots for $T_1 = T_{i_1} = 0.5105$keV, $n_1 = 0.2$cm^{-3}, $n_{i_1} = 1.6$cm^{-3}, and $\alpha = [0.1, 1, 2]$. T_2 and T_{i_2} vary between $T^* = 1.2$keV for silver and the SCATHA worst-case values $T_{2_{max}} = 24$keV and $T_{i_{2_{max}}} = 26$keV. These plots show the affect of varying T_2 on the equilibrium potentials of the spacecraft. In Figure 6a, $\alpha = 0.1$, and only 1 equilibrium potential exits for each value of T_2. It can also be observed that perturbations in T_2 cause the equilibrium potential to vary across all T_2, though to a greater degree when T_2 is close to T^*. As T_2 increases, the equilibrium potential decreases. The effect of perturbations in T_2 decrease as α increases. This can be seen in Figures 6b and 6c, which show the equilibrium surface plots for $\alpha = 1$ and $\alpha = 2$, respectively. For both plots, the equilibrium potential is constant for the majority of T_2. However, when T_2 is close to T^*, some variation can be discerned. The changes in the equilibrium potential are greater for $\alpha = 1$ than for $\alpha = 2$. These results support the conclusion that the electrostatic tractor is more effective when α is large, $n_1 \gg n_2$.

SPACECRAFT CHARGING IN KAPPA PLASMA

Particle Flux

The generalized Lorentzian, or kappa, VDF has been shown to adequately model suprathermal populations that are ubiquitous in the solar-wind and near-Earth space plasma.[20,24,38–41] The kappa VDF that describes the particle flux is[26]

$$f(E) = n \left(\frac{q_0}{2\pi\kappa T m}\right)^{1/2} \frac{E}{\kappa T} \left(\frac{\Gamma(\kappa+1)}{\Gamma(\kappa-1/2)}\right) \left(1 + \frac{E}{\kappa T}\right)^{-\kappa-1} \tag{8}$$

where $\Gamma(x)$ is the Gamma function and κ is the spectral index, which must be greater than 1. The value of κ determines the slope of the energy spectrum of the suprathermal particles forming the tail of the VDF.[20] The function becomes a Maxwellian as $\kappa \to \infty$. This can be seen in Figure 7, which shows the electron flux of a plasma using a kappa distribution. The Maxwellian distribution for the same environment is shown as a black, dashed line. The distributions for κs ranging from 2 to 50 are shown as multicolored solid lines. As the value of κ increases, the curves more closely resemble the Maxwellian curve.

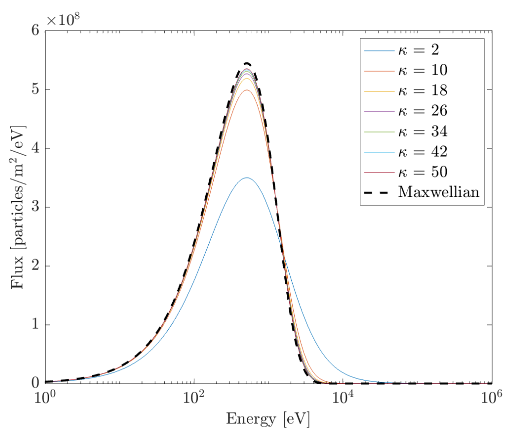

Figure 7: Electron flux vs. Energy using kappa distribution

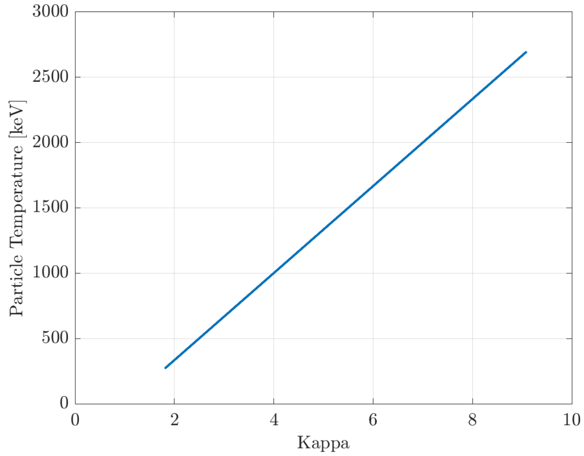

Figure 8: Charging threshold for kappa distribution

Charging Threshold

For the most part, the kappa distribution function behaves like a Maxwellian in terms of the charging threshold. In other words, the natural potential of the spacecraft will converge to either positive or negative depending solely on the intensity of ion contribution in the plasma relative to that of the electron contribution. The critical temperature T^* would still apply in an environment neglecting ions. This is opposed to the bi-Maxwellian function, which may jump between positive and negative potentials as a result of the electron density ratio in addition to the intensity of the ion contribution from both constituting populations of plasma. However, the suprathermal tails, which are the observed by the extension into higher energies in the curves with smaller values of κ, that are accounted for in the kappa function cause negative charging to begin at lower temperatures than for the Maxwellian function alone. This is visualized in Figure 8, in which the blue line denotes the onset of charging. Above the line, the spacecraft is charged to a positive potential. Below the line, the spacecraft is charged to a negative potential. The spacecraft is also charged to a negative potential beyond the extent of the line.

This threshold line is for the environment with $n = n_i = 0.2\text{cm}^{-3}$ and $T = T_i = 0.5105\text{keV}$, where the subscript i denotes the ion population. Both the electrons and ions are modeled using a kappa distribution function with the same κ. Lower values of κ indicate greater suprathermal tails, meaning that hotter deviations from thermal equilibrium are present. Higher values of κ behave more similarly to the Maxwellian. Because the electron mass (9.10938×10^{-31}kg) is orders of magnitude less than the ion mass (1.67262×10^{-27}kg), from Equation 8, the electron flux is much greater than the ion flux. It follows that lower values of κ induce negative charging at a lower temperature than at higher values of κ. It is also evident from Figure 8 that variations in κ change the temperature at which negative charging begins linearly: there is a linear relationship between κ and the temperature threshold for charging.

Active Spacecraft Charging

Figure 9 shows charging in the kappa plasma with various values of κ compared to charging in a single-Maxwellian plasma with the same plasma properties, neglecting the effects of the servicer, with electron beam current $I_{\text{beam}} = 50\mu\text{A}$. The plasma properties are $T = T_i = 0.5105\text{keV}$ and

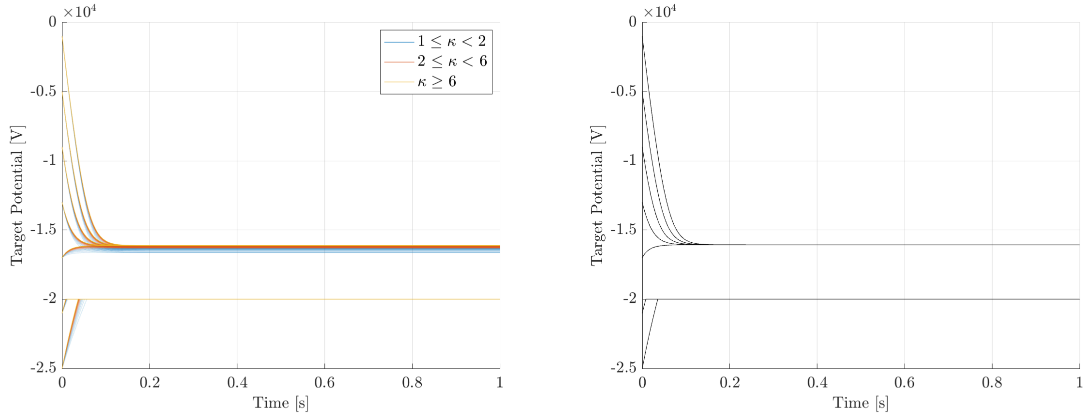

(a) Kappa plasmas

(b) Single-Maxwellian plasma

Figure 9: Active charging in kappa and single-Maxwellian plasmas, no servicer

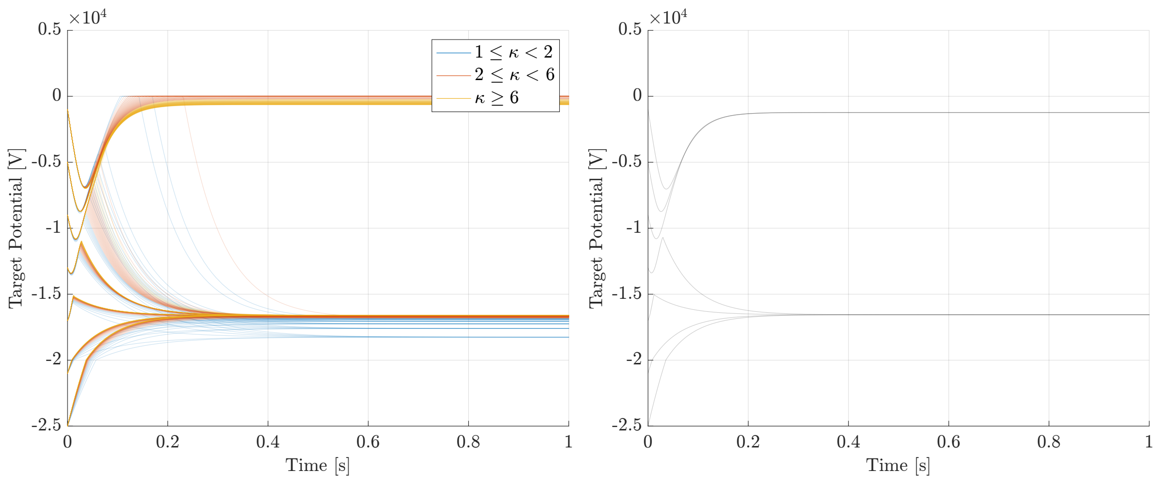

(a) Kappa plasmas

(b) Single-Maxwellian plasma

Figure 10: Active charging in kappa and single-Maxwellian plasmas, with servicer

$n = n_i = 0.2\text{cm}^{-3}$. Figure 9a illustrates the target potential over time with both electrons and ions modeled using a kappa distribution. The initial target potential ϕ_0 is at 10 linearly spaced values between -1keV to -25keV. For each ϕ_0, 50 linearly spaced κs between 1 and 10 are plotted. From the source of Equation 8, κ cannot be less than 1.[26] Values of κ between 1 and 2 are show in blue in Figure 9a. Previous research has found that kappa distributions with $2 < \kappa < 6$ fit the satellite data in the terrestrial magnetosphere,[39] the solar wind,[24,40] and other near-Earth space environments.[20] Values of κ between 2 and 6 are highlighted in orange in Figure 9a. Values of $\kappa > 6$ are shown in yellow. Figure 9b shows active charging in equivalent the single-Maxwellian environment for comparison, also with 10 linearly spaced values of ϕ_0 ranging from -1keV to -25keV.

It can be clearly observed in Figure 9 that charging in the kappa plasma is almost identical to charging in a single-Maxwellian plasma. For low values of κ, the least negative equilibrium potential shifts slightly more negative, and it takes slightly longer to converge to the most negative equilibrium potential. For the expected distributions in the near-Earth environment $2 \leq \kappa < 6$, the result of active charging is near indistinguishable from the single-Maxwellian.

The variations in κ have a more dramatic effect when including the servicer, as shown in Figure 10. In general, it can be observed that the target potential over time in the kappa plasma follows the same pattern as the single-Maxwellian plasma, similar to Figure 9 without the servicer. However, including the servicer as in Figure 10 causes higher values of κ to be required in order to converge to the least-negative equilibrium potential. For lower values of κ, including much of $2 \leq \kappa < 6$, it is even possible to converge to a positive potential. It is important to note that the material used in these simulations is silver, whose material properties make it more prone to the positive charging influenced by the ambient environment. Other materials, such as aluminum, would have different resulting potentials and may not converge to a positive value at all. Interestingly, it is the distributions with lower values of κ (greater suprathermal tails) that consistently charge negatively, which is required by the electrostatic tractor concept. Even for less negative values of ϕ_0, smaller κs converge to the most negative equilibrium. The caveat is that there is some variation in where that most negative equilibrium lies when κ is small, similar to what was observed when α was small in the double-Maxwellian environment. This indicates that variations in the suprathermal tails could result in jumps in the equilibrium potential, making charging using the electrostatic tractor difficult to predict.

SPACECRAFT CHARGING IN PLASMA WITH MAXWELLIAN CORE AND KAPPA HALO

Particle Flux

The phrasing "Maxwellian core and kappa halo" is intended to imply that the cooler population 1 particles are modeled using a Maxwellian distribution and the hot population 2 particles are modeled using a kappa distribution function. As a result, the Maxwellian core and kappa halo has a particular case that is a bi-Maxwellian distribution as $\kappa \to \infty$. The VDF of the Maxwellian core and kappa halo is then

$$f(E) = f_1(E) + f_2(E) \tag{9a}$$

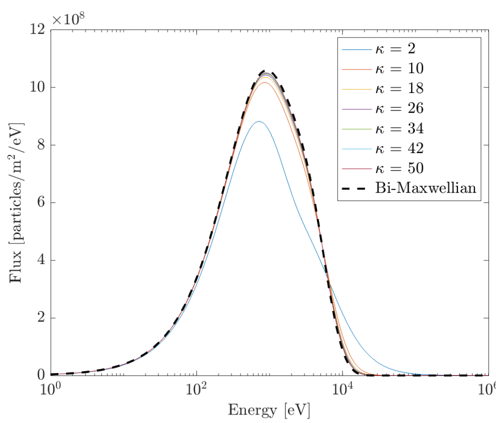

(a) Total flux

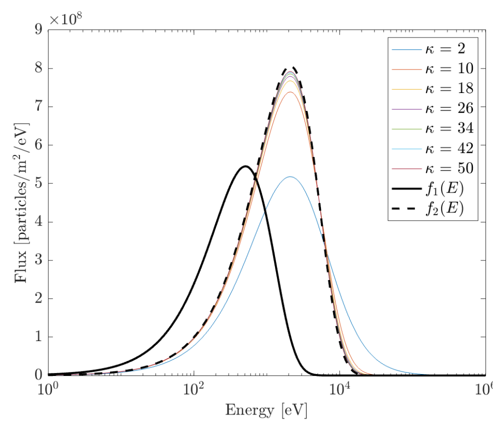

(b) Deconstructed flux

Figure 11: Electron flux of plasma with Maxwellian core and kappa halo

$$f_1(E) = n_1 \left(\frac{q_0}{2\pi m T_1}\right)^{1/2} \frac{E}{T_1} \exp\left(-\frac{E}{T_1}\right) \tag{9b}$$

$$f_2(E) = n_2 \left(\frac{q_0}{2\pi \kappa T_2 m}\right)^{1/2} \frac{E}{\kappa T_2} \left(\frac{\Gamma(\kappa+1)}{\Gamma(\kappa-1/2)}\right) \left(1 + \frac{E}{\kappa T_2}\right)^{-\kappa-1} \tag{9c}$$

where $f(E)$ is the total flux, $f_1(E)$ uses a Maxwellian flux distribution, and $f_2(E)$ uses a kappa flux distribution.

Figure 11 illustrates the electron flux distribution of the Maxwellian core and kappa halo distribution compared to a bi-Maxwellian distribution. The environment used here is the same as the mild environment shown in Table 1, with κ varying incrementally between 2 and 50 for population 2. Figure 11a shows the total flux, while Figure 11b shows the population 1 flux $f_1(E)$ and the population 2 flux $f_2(E)$ individually. In Figure 11a, it can easily be observed that as κ becomes increasingly large, the flux of the Maxwellian core and kappa halo plasma converges to the bi-Maxwellian distribution, which is shown as a black, dashed line. In Figure 11b, the suprathermal tails in the population 2 flux are seen and the flux converges to the Maxwellian black, dashed line as $\kappa \to \infty$. The Maxwellian population 1 flux is shown as a black, solid line.

Active Spacecraft Charging

It follows from the findings in the previous section that active charging in the Maxwellian core and kappa halo environment would closely resemble active charging in a bi-Maxwellian environment, with variation relating to increased suprathermal tails in population 2. Figure 12a makes this comparison by showing target potential over time for the Maxwellian core and kappa halo environment plotted together with the results for the same bi-Maxwellian environment. In this figure, the mild spacecraft environment shown in Table 1 is used. Note that the electron density ratio α is $\frac{1}{3}$ for the mild environment. The effects of the servicer are initially omitted for clearer discussion. For the case $1 \leq \kappa < 2$, the lines are drawn in blue. The expected near-Earth or solar wind suprathermal tails $2 \leq \kappa < 6$ are highlighted in orange. The case where $\kappa \geq 6$ is drawn in yellow, and the bi-Maxwellian result is shown in black. Figure 12b paints a full picture of active charging by showing

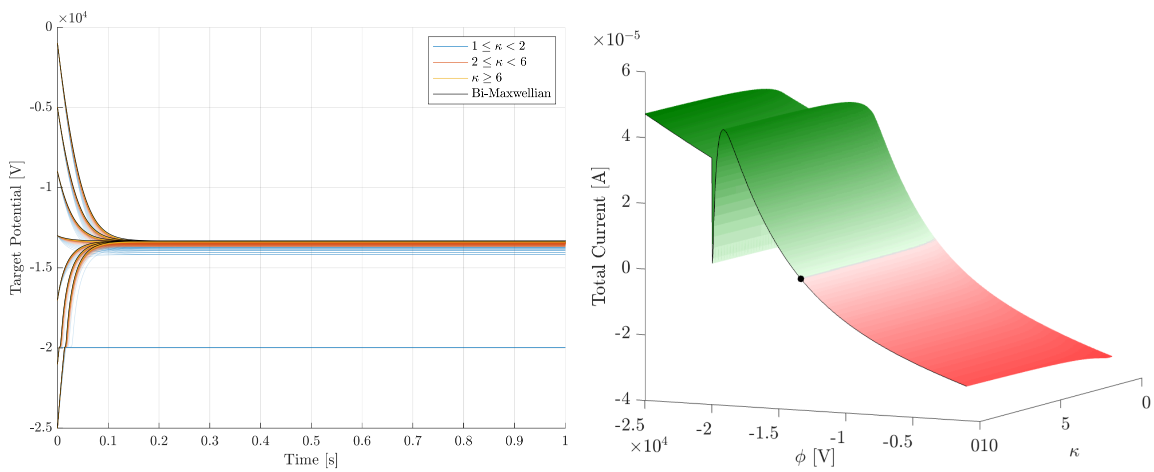

(a) Target potential vs. time

(b) Total current vs. potential and κ

Figure 12: Active charging in mild environment with kappa halo, neglecting servicer

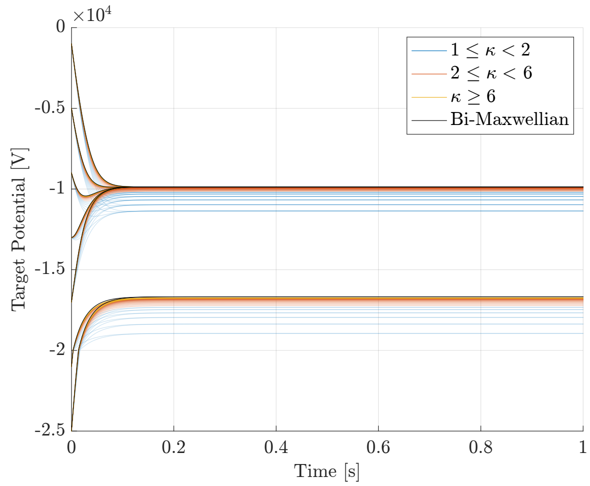

Figure 13: Active charging in mild environment with kappa halo, including servicer

the total current acting on the target as a function of the target potential and κ. It can be observed that for most values of κ, there are is only 1 equilibrium potential. This means that the environment and electron beam do not meet the requirements for multiple equilibria as described by Hammerl and Schaub.[29] However, as κ becomes small, the total current surface dips below zero, meaning that the aforementioned requirements for multiple equilibria are met. This change is notable because it means that variations in the suprathermal deviations from the Maxwellian may change the number of possible equilibria for a particular environment, and consequently may result in significant jumps in potential.

The full charging scenario for the mild environment including the effects from the servicer is shown in Figure 13. It can be observed that including the servicer causes the criteria for multiple equilibria to be met in every case. Similarly to when α was small in the bi-Maxwellian discussion, the equilibrium potential varies more significantly when κ is small, and it converges to a particular value as $\kappa \to \infty$. Recall that $\alpha = \frac{1}{3}$ for the mild environment. It is known from the bi-Maxwellian discussion that $\alpha < 1$ can cause severe jumps in target potential when the environment is perturbed. When n_2 is changed from 0.6cm^{-3} to 0.1cm^{-3} such that $\alpha = 2$, the effects are as expected. As seen in Figure 14, greater suprathermal tails (smaller κ) have less of an effect on the equilibrium potential as they did when α was small. Of course, this is a result of a less dense n_2, so the population 2 flux, which is modeled using a kappa distribution, has less of an effect on the charging of the spacecraft.

RESULTING FORCES AND TORQUES

For two spheres in proximity of one another with radii R_1 and R_2, potentials V_1 and V_2, charges q_1 and q_2, and separated by a distance d, the charges can be related to the potentials using

$$\begin{bmatrix} V_1 \\ V_2 \end{bmatrix} = k_c \begin{bmatrix} 1/R_1 & 1/d \\ 1/d & 1/R_2 \end{bmatrix} \begin{bmatrix} q_1 \\ q_2 \end{bmatrix} \tag{10}$$

where k_c is the Coloumb constant equal to 8.988×10^9 (N·m^2)/C^2. Then the electrostatic force between them can be calculated easily using Coloumb's Law.

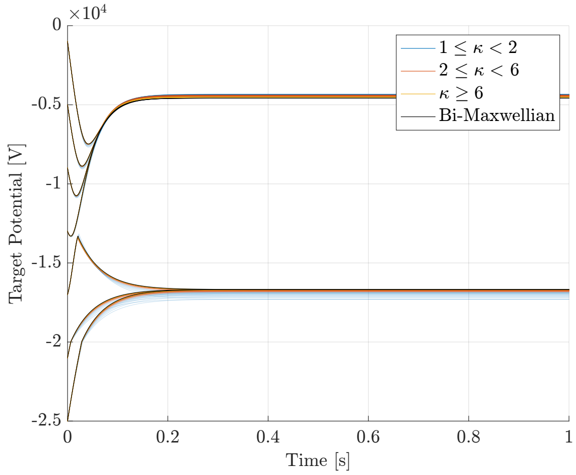

(a) Target potential vs. time

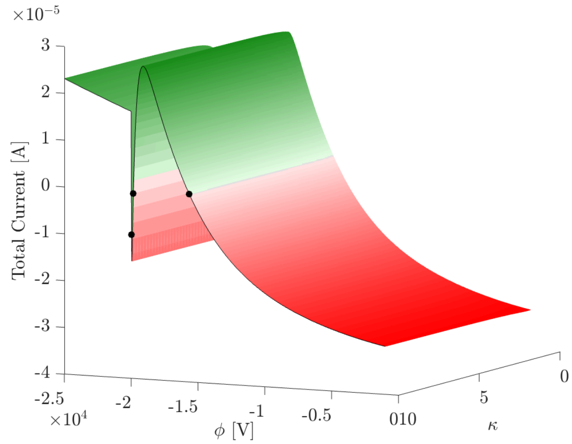

(b) Total current vs. potential and κ

Figure 14: Active charging with $\alpha = 2$ and kappa halo, including servicer

$$F = k_c \frac{q_1 q_2}{d^2} \tag{11}$$

However, the forces and torques acting on a spacecraft cannot be accurately modeled when representing the 3D geometry as a sphere. As a result, the forces and torques on the target resulting from the equilibrium potentials for each of the three GEO environment models is calculated using the surface multi-sphere method (MSM). The surface MSM can analytically approximate the Coulomb interaction between charged bodies using a collection of finite spheres placed homogeneously along the surface of the spacecraft to represent a complex shape.[42,43] For n spheres making up a single spacecraft, Equation 10 becomes

$$\begin{bmatrix} V_1 \\ V_2 \\ \vdots \\ V_n \end{bmatrix} = k_c \begin{bmatrix} 1/R_1 & 1/d_{1,2} & \cdots & 1/d_{1,n} \\ 1/d_{2,1} & 1/R_2 & \cdots & 1/d_{2,n} \\ \vdots & \vdots & \ddots & \vdots \\ 1/d_{n,1} & 1/d_{n,2} & \cdots & 1/R_n \end{bmatrix} \begin{bmatrix} q_1 \\ q_2 \\ \vdots \\ q_n \end{bmatrix} \tag{12}$$

which can be written simply as

$$\boldsymbol{V} = [S]\boldsymbol{Q} \tag{13}$$

where $[S]$ is the elastance matrix. Now, for two charged bodies represented by multiple spheres, Equation 13 has the form

$$\begin{bmatrix} \boldsymbol{V}_1 \\ \boldsymbol{V}_2 \end{bmatrix} = \begin{bmatrix} S_1 & S_M \\ S_M^T & S_2 \end{bmatrix} \begin{bmatrix} \boldsymbol{Q}_1 \\ \boldsymbol{Q}_2 \end{bmatrix} \tag{14}$$

where S_M is the mutual capacitance block of the elastance matrix, which changes with the relative position of the two bodies.[44] Finally, the force and torque acting on body 1, which is composed of n spheres, about a point P can be calculated by

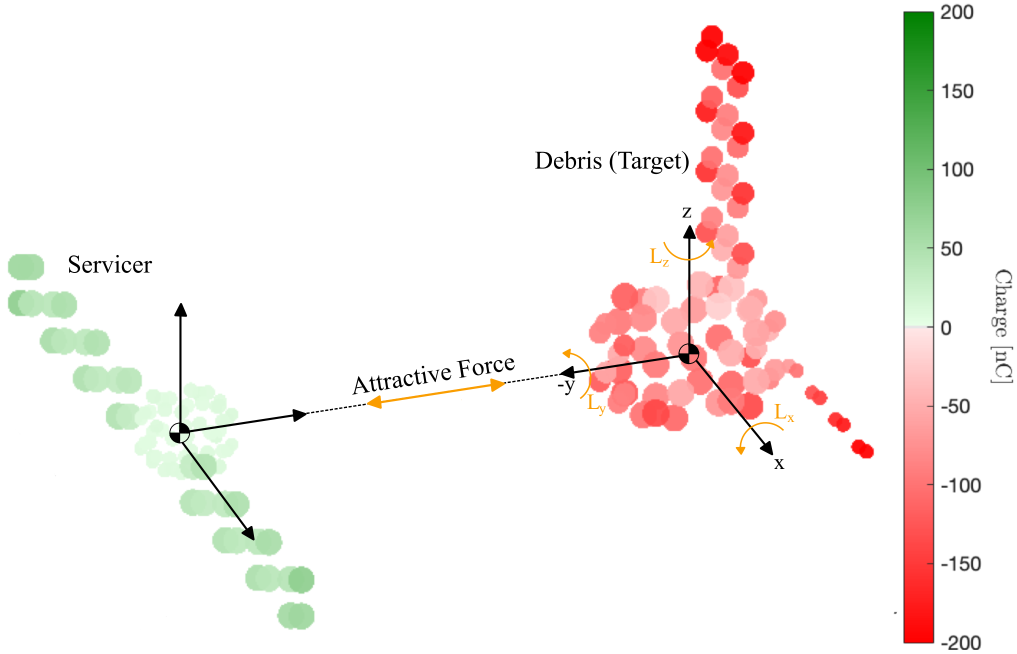

Figure 15: Depiction of the multi-sphere method

$$\mathbf{F}_1 = k_c \sum_{j=1}^{n} \mathbf{Q}_{1_j} \left(\sum_{i=1}^{n} \frac{\mathbf{Q}_{2_i}}{r_{i,j}^3} \mathbf{r}_{i,j} \right) \tag{15}$$

and

$$\mathbf{L}_{1,P} = k_c \sum_{j=1}^{n} \mathbf{r}_j \times \mathbf{F_1} \tag{16}$$

where $\mathbf{r}_j$ is the vector from P to the jth sphere.

Figure 15 shows the spacecraft models used in this analysis, representing both the target and servicer spacecraft using the MSM with 80 spheres. The later calculations use 20 spheres to reduce the computational complexity, but the visualization uses 80 spheres for clarity. The target spacecraft on the right is represented using a GOES-R satellite, which was selected for its asymmetric shape resulting from a single 5m $\times$ 10m solar panel and its 10m long magnetometer. The bus of the GOES-R satellite is a 4m $\times$ 4m $\times$ 6m cuboid. The servicer spacecraft is represented by a 2.5m $\times$ 2.5m $\times$ 3m SSL-1300 satellite bus with two 3m $\times$ 14m solar panels. The spacecraft are located 20m apart in the y direction. Figure 15 also shows that the MSM calculates the charge on each sphere. This is a particular instance of a right-hand equilibrium potential in the mild bi-Maxwellian environment. Positive charges are shown in green and negative charges are shown in red. Greater magnitudes of charge are shown in shades with greater intensity, and vice versa. It can be observed that the charge magnitudes are greater on the outer spheres making up the spacecraft. The components of the torque on the target are shown in orange on the figure. The servicer also experiences torques, but this analysis focuses on the results of the target.

Bi-Maxwellian Distribution

Figure 16 illustrates the forces and torques in the mild bi-Maxwellian environment using the MSM from $\phi_0 = -1$keV, which converge primarily to the right-side equilibria, and $\phi_0 = -25$keV, which converge primarily to the left-side equilibria. The phrasing "right-side" equilibrium refers to the least negative equilibrium potential and "left-side" equilibrium refers to the most negative equilibrium potential for cases where there are multiple equilibria in a particular environment. If there is only one equilibrium, then that equilibrium potential is the right-side equilibrium. In Figure 16, the electron density ratio α varies as in Figure 4, and the force and torque components on the target are calculated and plotted for each environment. Figure 16a and 16b show the results for $\phi_0 = -1$keV and Figure 16c and 16d show the results for $\phi_0 = -25$keV. It is not important to show results for other initial target potentials because ϕ_0 only affects whether the potential will converge to the right- or left-side equilibrium, if there are multiple equilibria. It is α that dictates the value of those equilibria.

The immediate observations are as expected: small values of α result in forces and torques very different from the larger values of α, and as $\alpha \to \infty$ the forces and torques experienced by the target converge. These findings reflect the results of the equilibrium potentials in Figure 4. Additionally,

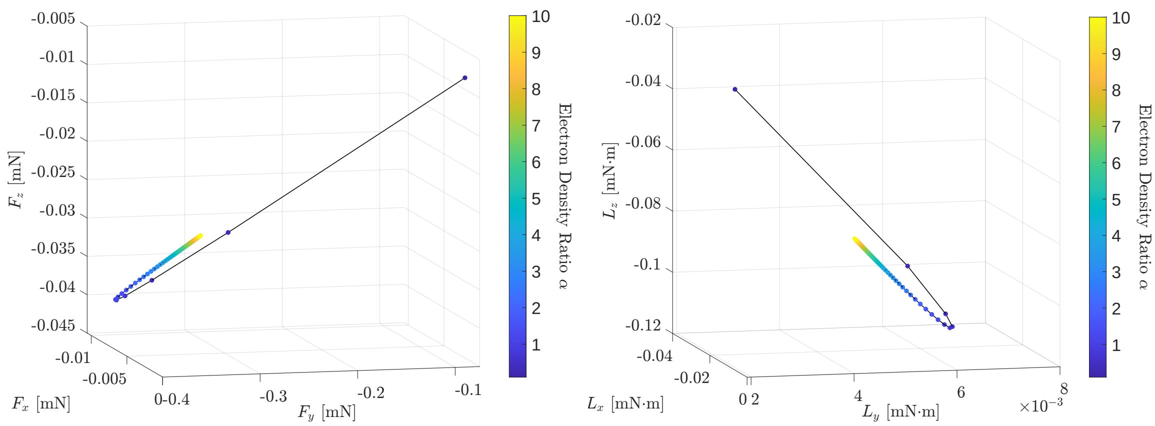

(a) Forces from $\phi_0 = -1$keV **(b)** Torques from $\phi_0 = -1$keV

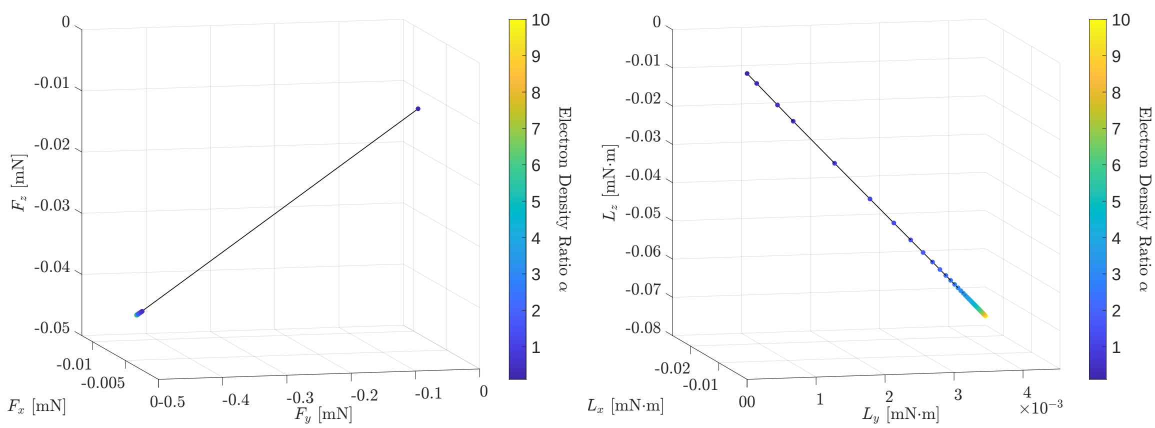

(c) Forces from $\phi_0 = -25$keV **(d)** Torques from $\phi_0 = -25$keV

Figure 16: Forces and torques in the mild bi-Maxwellian environment at each α

there is significantly more variation in the right-side results than in the left-side results, which again reflects the potentials that are observed in Figure 4. In Figures 16c and 16d, it can be observed that there is one point representing $\alpha = 0.1$ located far from the cluster of other points that represent larger values of α. This is the case where the environment changes such that there is only one equilibrium point, so the potential converges to a right-hand equilibrium. An interesting finding in Figures 16a and 16b is that the y- and z-components of the force acting on the target initially decrease quickly as α increases before reaching a minimum and increasing slowly. Since the x-component of the force increases initially as α increases, this corresponds to an increase in the y-component of torque. Of course, different orientations of each spacecraft will vary the components of torque that are modified due to the resulting forces.

In the SCATHA worst-case bi-Maxwellian environment, there is only one equilibrum potential for each α, so it is not necessary to show the force and torque results at more than one ϕ_0. Figure 17 shows forces and torques resulting from the potentials computed in Figure 5 for $\phi_0 = -1$keV. Recall that for small values of α, the potential converges to a slightly positive equilibrium. Interestingly, only the smallest value of α in this analysis ($\alpha = 0.1$) results in a repulsive force. Moreover, the force is so small (on the order of 10^{-11}N in the y direction), that it can be considered negligible. Thus, while the electrostatic tractor would be unable to pull the target debris object in such an environment, it would not end up pushing the object away from it. In Figure 5, there are 4 values of α that produce positive potentials, but 3 of them still generate attractive forces. This is due to the large electric field produced by the servicer spacecraft relative to that produced by the target, which causes induced charging effects that make the charge on the target negative despite having a positive potential.[45] The effects of the electric fields from one spacecraft on another is a function of separation distance and electric potential.[45] In this case, the equilibrium potential of the servicer in these 3 cases is on the order of 1000s of volts while the target potential is on the order of a few volts or or less, so induced charging effects occur. In the case where the resulting force is repulsive, the potentials of both the target and servicer are on the order of several V. It should also be noted that the forces resulting from the case where both the target and servicer potentials have the same sign are less than when they have opposite signs.[45]

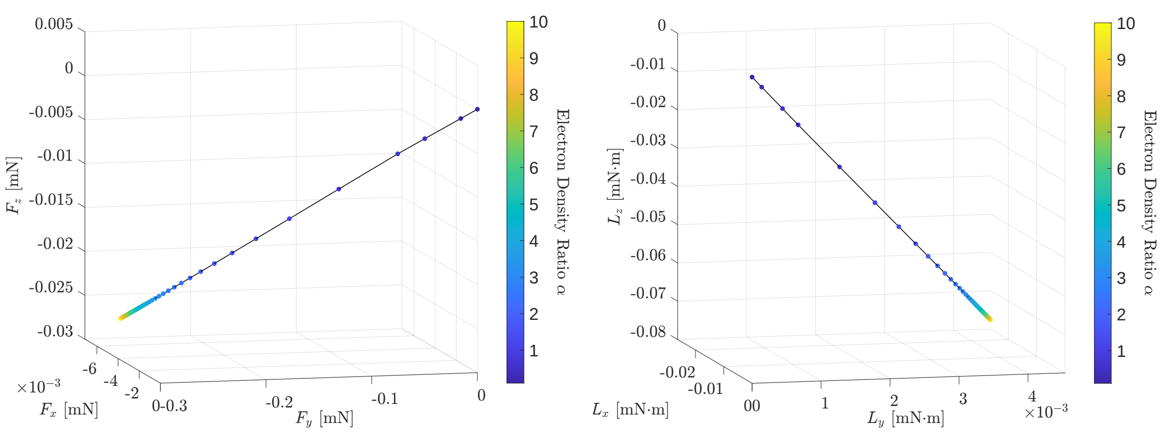

(a) Forces from $\phi_0 = -1$keV

(b) Torques from $\phi_0 = -1$keV

Figure 17: Forces and torques in the worst-case bi-Maxwellian environment at each α

Kappa Distribution

Figure 18 illustrates the forces and torques in the kappa environment using the MSM from $\phi_0 = -1$keV and $\phi_0 = -25$keV. The value of κ varies as in Figure 10, and the force and torque components on the target are calculated and plotted for each environment.

It is known from Figure 10 that for $\phi_0 = -1$keV, while larger value of κ all converge to the right-side equilibria, some smaller values converge to the left-side equilibria. For $\phi_0 = -25$keV, all values of κ converge to the left-side equilibria. This can be easily seen in Figure 18. In Figures 18a and 18b, as κ increases from its minimum, the force and torque begin to converge to those that result from the left-side equilibrium. There is then a sudden jump to a force and torque from a right-side potential, which converges to the force and torque resulting from the single-Maxwellian right-side equilibrium. In Figure 10, it can be observed that the jump to the right-side equilibria results in a potential that is initially positive, but eventually becomes negative again as κ continues to increase. However, the force between the spacecraft is always attractive. This is again a result of the large electric field generated by the servicer, which has a potential magnitude that is significantly greater than that of the target when they are both positive. This phenomenon is also the explanation for the sharp turn experienced by force and torque in Figures 18a and 18b. At the point where the electric

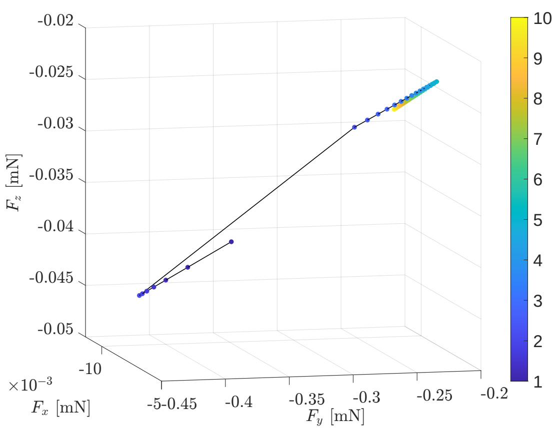

(a) Forces from $\phi_0 = -1$ keV

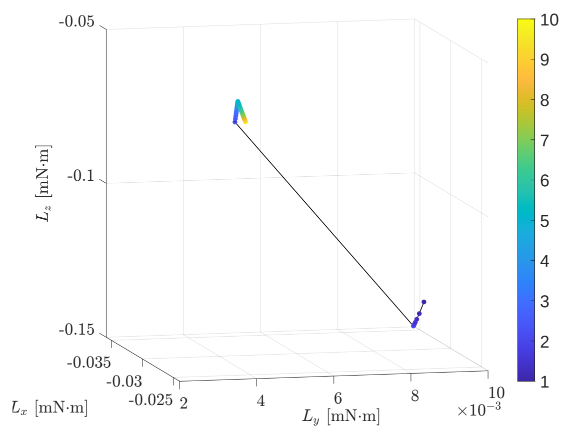

(b) Torques from $\phi_0 = -1$ keV

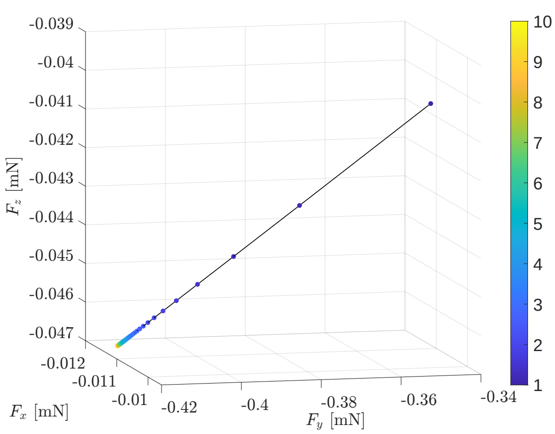

(c) Forces from $\phi_0 = -25$ keV

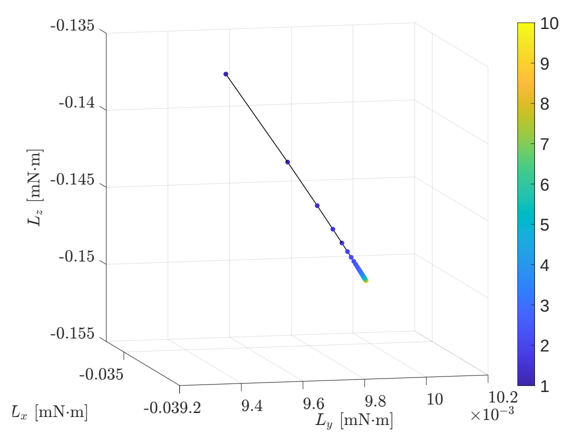

(d) Torques from $\phi_0 = -25$ keV

Figure 18: Forces and torques in the kappa environment at each $\boldsymbol{\kappa}$

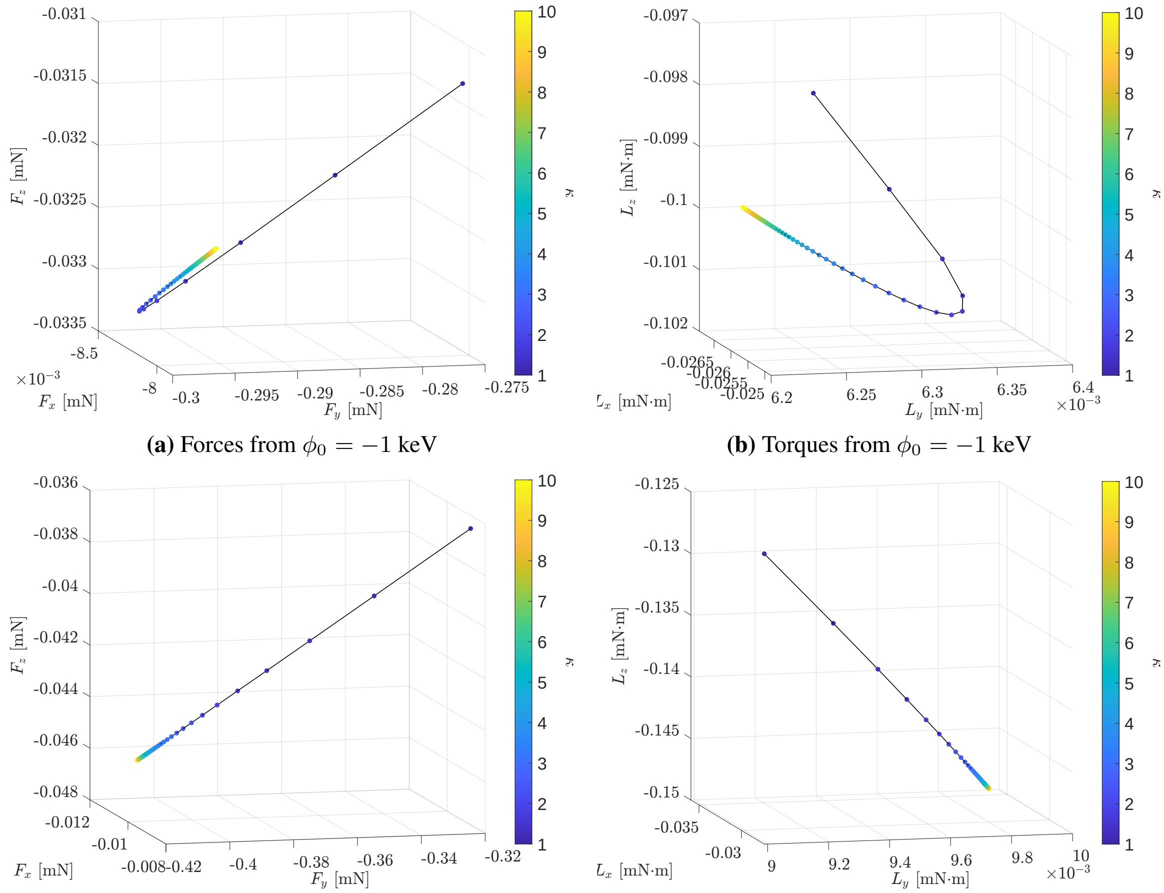

(a) Forces from $\phi_0 = -1$ keV

(b) Torques from $\phi_0 = -1$ keV

(c) Forces from $\phi_0 = -25$ keV

(d) Torques from $\phi_0 = -25$ keV

Figure 19: Forces and torques in the Maxwellian core kappa halo environment at each $\boldsymbol{\kappa}$

potential of the target becomes negative again, the induced charging effects from the servicer's electric field are no longer felt and the dynamics of charge accumulation changes. In Figures 18c and 18d, all values of κ produce forces and torques from the left-side equilibria. As κ increases, the force and torque converges to those that result from the single-Maxwellian left-side equilibrium. Small values of κ result in jumps in the force felt on the object. Since the magnitudes are not very large to begin with, the jumps may not have a significant impact on the control of the electrostatic tractor.

Maxwellian Core and Kappa Halo Distribution

Figure 19 shows the resulting forces and torques in the Maxwellian core and kappa halo environment using the properties of the mild bi-Maxwellian environment seen in Table 1, corresponding to the potentials in Figure 13. The value of κ varies through 50 linearly spaced values from 1 to 10, and the force and torque components on the target are calculated and plotted for each environment. It is important to note that for this environment, all of $\phi_0 = -1$keV converge to the right-side equilibria, and all of $\phi_0 = -25$keV converge to the left-side equilibria. Thus, Figures 19a and 19b are the forces and torques resulting from the right-side equilibria and Figures 19c and 19d are the forces and torques resulting from the left-side equilibria.

For both the right- and left-side equilibrium potentials, the resulting forces and torques converge to a particular value as κ increases. When κ is small, the force and torque experienced by the target may jump on the order of tenths of mN and hundredths of mN·m. The forces resulting from the right-side equilibria have the interesting property seen previously in Figure 16. In this case, as κ increases, the forces in the y and z directions quickly become more negative before turning around and slowly increasing. The resulting torque corresponds to this variation in the force components.

CONCLUSION

This research investigates active spacecraft charging in various non-Maxwellian GEO environments and computes the forces and torques generated by the resulting equilibrium potentials. The environments are modeled by a bi-Maxwellian distribution, a kappa distribution, and a distribution made up of a cooler Maxwellian core and a hotter kappa halo. It is found that for both the mild and worst-case bi-Maxwellian environments, the equilibrium potential experiences significant jumps due to perturbations in the environment when the electron density ratio α is small and converges to a particular value as $\alpha \to \infty$. For the worst-case environment, it is possible for the target to become charged to a positive potential even in the presence of an electron beam current of 50μA when α is small. It was originally predicted that this could impede the function of the electrostatic tractor since the servicer is also charged positively. However, it is concluded that for most cases, the target will still have a negative charge distributed along its surface due to induced charging effects from the servicer's significant electric field, thus resulting in an attractive force between the target and servicer. For the kappa environment, it was observed that as $\kappa \to \infty$, the active charging behaves like that for a single-Maxwellian plasma. When κ is small, jumps in the equilibrum potential are more likely to occur. In fact, a diminishing κ can induce a jump from the right-side equilibrium potential to the left-side equilibrium potential. This is reflected in the resulting forces and torques, which show that as κ increases, the force begins to converge and then jumps significantly before converging again. In the environment tested in this analysis, the jump from the left- to right- side equilibrium results in a positive potential, but the charge distributed along the surface of the target remains negative due to induced charging effects from the servicer's electric field. The Maxwellian core and kappa halo environment has the property that as $\kappa \to \infty$, the distribution function is bi-Maxwellian. It is found that variations in κ may cause jumps in the equilibrium potential, including a possibility of inducing multiple equilibria in an environment that previously had only one. The forces and torques show that the jumps are more significant when κ is small.

ACKNOWLEDGEMENT

The authors would like to thank Julian Hammerl for his spacecraft charging model and his assistance using the multi-sphere method. The authors would also like to thank Kaylee Champion for her assistance acquiring NASCAP material properties. This work was supported by the U.S. Air Force Office of Scientific Research under grant FA9550-23-S-0570.

REFERENCES

[1] "IADC Space Debris Mitigation Guidelines," tech. rep., Inter-Agency Debris Coordination Committee, 2007.

[2] H. Schaub, L. E. Jasper, P. V. Anderson, and D. S. McKnight, "Cost and risk assessment for spacecraft operation decisions caused by the space debris environment," *Acta Astronautica*, 2015.

[3] P. de Selding, "FCC Enters Orbital Debris Debate," *Space News Business Report*, 2004.

[4] D. Shepardson, "DISH gets first-ever space debris fine over EchoStar-7," *Reuters*, 2023.

[5] H. Zhang, Z. Li, W. Wang, Y. Zhang, and H. Wang, "Geostationary orbital debris collision hazard after a collision," *Aerospace*, Vol. 9, 2022, p. 258.

[6] D. L. Oltrogge, S. Alfano, C. Law, A. Cacioni, and T. S. Kelso, "A comprehensive assessment of collision likelihood in Geosynchronous Earth Orbit," *Acta Astronautica*, Vol. 147, 2018, pp. 316–345.

[7] D. Reintsema, J. Thaeter, A. Rathke, *et al.*, "DEOS – The German Robotics Approach to Secure and De-Orbit Malfunctioned Satellites from Low Earth Orbits," *i-SAIRAS 2010*, Aug. 2010.

[8] R. Biesbroek, S. Aziz, A. Wolahan, *et al.*, "The Clearspace-1 Mission: ESA and Clearspace Teap Up To Remove Debris," *8th European Conference on Space Debris*, Apr. 2021.

[9] S.-I. Nishida and S. Kawamoto, "Strategy for capturing of a tumbling space debris," *Acta Astronautica*, Vol. 68, No. 1-2, 2011, pp. 113–120.

[10] K. Stadnyk, K. Hovell, and L. Brewster, "Space Debris Removal With Sub-Tethered Net: A Feasibility Study and Preliminary Design," *8th European Conference on Space Debris*, Apr. 2021.

[11] R. Dudziak, S. Tuttle, and S. Barraclough, "Harpoon technology development for the active removal of space debris," *Advances in Space Research*, Vol. 56, Aug. 2015, pp. 509–527.

[12] G. S. Aglietti, B. Taylor, S. fellowes, *et al.*, "The active space debris removal mission RemoveDebris. Part 2: In orbit operations," *Acta Astronautica*, Vol. 168, Mar. 2020, pp. 310–322.

[13] P. Papushev, Y. Karavaev, and M. Mishina, "Investigations of the evolution of optical characteristics and dynamics of proper rotation of uncontrolled geostationary artificial satellites," *Advances in Space Research*, Vol. 43, 2009, pp. 1416–1422.

[14] Y. Karavaev, R.M.Kopyatkevich, M. Mishina, G. Mishin, P. Papushev, and P. Shaburov, "The dynamic properties of rotation and optical characteristics of space debris at geostationary orbit," *Advances in the Astronautical Sciences*, 2004, p. 1457–1466.

[15] E. H. Trevor Bennett, Daan Stevenson and H. Schaub, "Prospects and challenges of touchless electrostatic detumbling of small bodies," *Advances in Space Research*, Vol. 56, 2015, pp. 557–568.

[16] H. Schaub and J. D. F. Moorer, "Geosynchronous large debris reor- biter: Challenges and prospects," *The Journal of Astronautical Sciences*, Vol. 59, 2012, pp. 161–176.

[17] K. Champion and H. Schaub, "Electrostatic Potential Shielding in Representative Cislunar Regions," *IEEE TRANSACTIONS ON PLASMA SCIENCE*, Vol. 51, 2023.

[18] G. D. R. Chao-Song Huang, *Multiscale Coupling of Sun-Earth Processes*. Elsevier, 2005.

[19] I. Batista, E. d. Paula, M. Abdu, N. Trivedi, and M. Greenspan, "Ionospheric effects of the March 13, 1989, magnetic storm at low and equatorial latitudes," *Journal of Geophysical Research*, Vol. 96, 08 1991, pp. 13943–13952, 10.1029/91JA01263.

[20] V. Pierrard and M. Lazar, "Kappa Distributions: Theory and Applications in Space Plasmas," *Solar Physics*, 2010.

[21] M. D. Montgomery, S. J. Bame, and A. J. Hundhausen, "Solar wind electrons: Vela 4 measurements," *Journal of Geophysical Research*, 1968.

[22] W. C. Feldman, J. R. Asbridge, S. J. Bame, M. D. Montgomery, and S. P. Gary, "Solar wind electrons," *Journal of Geophysical Research*, 1975.

[23] W. G. Pilipp, H. Miggenrieder, M. D. Montgomery, K. H. Mühlhäuser, and H. R. a. R. Schwenn, "Characteristics of electron velocity distribution functions in the solar wind derived from the Helios Plasma Experiment," *Journal of Geophysical Research*, 1987.

[24] V. P. Milan Maksimovic and P. Riley, "Ulysses electron distributions fitted with Kappa functions," *Journal of Geophysical Research*, 1997.

[25] I. Zouganelis, "Measuring suprathermal electron parameters in space plasmas: Implementation of the quasi-thermal noise spectroscopy with kappa distributions using in situ Ulysses/URAP radio measurements in the solar wind," *Journal of Geophysical Research*, 2008.

[26] V. Davis, B. Gardner, and M. Mandell, "Nascap-2k version 4.3 users manual," *Leidos Holdings San Diego, CA, USA, Tech. Rep. AFRL-RVPS-TR-2017-0002*, 2016.

[27] E. Mullen, M. Gussenhoven, and H. Garrett, "A "Worst Case" Spacecraft Environment as Observed by SCATHA on 24 April 1979," *Environmental Research Papers*, No. 751, 1981.

[28] M. H. Denton, M. F. Thomsen, H. Korth, S. Lynch, J. C. Zhang, and M. W. Liemohn, "Bulk plasma properties at geosynchronous orbit," *Journal of Geophysical Research: Space Physics*, 2005.

[29] J. Hammerl and H. Schaub, "Coupled Spacecraft Charging Due to Continuous Electron Beam Emission and Impact," *Journal of Spacecraft and Rockets*, 2024.

[30] E. C. Whipple Jr., *The equilibrium electric potential of a body in the upper atmosphere and in interplanetary space*. PhD thesis, George Washington University, 1965.

[31] C. Nam, N. Hershkowitz, M. H. Cho, T. Intrator, and D. Diebold, "Multiple valued floating potentials of Langmuir probes," *Journal of Applied Physics*, Vol. 63, 1988, pp. 5674–5677.

[32] N. L. Sanders and G. T. Inouye, "Secondary Emission Effectson Spacecraft Charging: Energy Distribution Consideration," *Spacecraft Charging Technology—1978*, 1979.

[33] S. M. Prokopenko and J. G. L. Laframboise, "High Voltage Differential Charging of Geostationary Spacecraft," *Journal of Geophysical Research*, Vol. 85, 1980.

[34] S. T. Lai, *Fundamentals of Spacecraft Charging*. Princeton University Press, 2012.

[35] S. Ali, N. Rubab, K. Nawaz, and S. Sawar, "A Comparative Study of Spacecraft Charging Onset at Geosynchronous Altitudes: A Nonextensive Particle Approach," *Journal of Geophysical Research: Space Physics*, 2020.

[36] J. Huang, G. Liu, and L. Jiang, "Threshold for spacecraft charging in double-Maxwellian plasma," *Journal of Geophysical Research: Space Physics*, Vol. 120, 2015, p. 6301–6308.

[37] J. Huang, G. Liu, and L. Jiang, "Theory of spacecraft potential jump 10.1002/2015JA021820 in geosynchronous plasma," *Journal of Geophysical Research: Space Physics*, 2015.

[38] V. M. Vasyliunas, "A survey of low-energy electrons in the evening sector of the magnetosphere with OGO 1 and OGO 3," *Journal of Geophysical Research*, 1968.

[39] G. Gloeckler and D. C. Hamilton, "AMPTE Ion Composition Results," *Physica Scripta*, 1987.

[40] G. Gloeckler, J. Geiss, H. Balsiger, P. Bedini, J. Cain, J. Fischer, *et al.*, "The Solar Wind Ion Composition Spectrometer," *Astronomy and Astrophysics Supplement Series*, 1992.

[41] I. Zouganelis, M. Maksimovic, N. Meyer-Vernet, H. Lamy, and K. Issautier, "A Transonic Collisionless Model of the Solar Wind," *The Astrophysical Journal*, 2004.

[42] D. Stevenson and H. Schaub, "Multi-sphere method for modeling spacecraft electrostatic forces and torques," *Advances in Space Research*, 2013.

[43] J. A. Hughes and H. Schaub, "Heterogeneous surface Multisphere models using method of moments foundations," *Journal of Spacecraft and Rockets*, 2013.

[44] J. Hammerl and H. Schaub, "Effects of Electric Potential Uncertainty on Electrostatic Tractor Relative Motion Control Equilibria," *Journal of Spacecraft and Rockets*, 2022.

[45] H. Schaub and L. E. Z. Jasper, "Orbit Boosting Maneuvers for Two-Craft Coulomb Formations," *Journal of Guidance, Control, and Dynamics*, 2013.